A New Approach for Broken Rotor Bar Detection in Induction Motors Using Frequency Extraction in Stray Flux Signals

Panagiotis A. Panagiotou, Ioannis Arvanitakis, Neophytos Lophitis, *Member, IEEE*, Jose A. Antonino-Daviu, *Senior Member, IEEE* and Konstantinos N. Gyftakis, *Member, IEEE*

***Abstract*— This work offers a reliable solution to the detection of broken rotor bars in induction machines with a novel methodology, which is based on the fact that the fault related harmonics will have oscillating amplitudes due to the speed ripple effect. The method consists of two main steps: Initially, a time-frequency transformation is used and the focus is given on the steady-state regime; thereupon, the fault related frequencies are handled as periodical signals over time and the classical Fast Fourier Transform is used for the evaluation of their own spectral content. This leads to the discrimination of sub-components related to the fault and evaluation of their amplitudes. The versatility of the proposed method relies on the fact that it reveals the aforementioned signatures to detect the fault, regardless of the spatial location of the broken rotor bars. Extensive finite element simulations on a 1.1MW induction motor and experimental testing on a 1.1kW induction motor lead to the conclusion that, the method can be generalized on any type of induction motor independently from the size, power, number of poles and rotor slot numbers.**

***Index Terms*— broken bars, frequency extraction, induction motor, time-frequency, spectral content, stray flux**

I. Introduction

THE fact that induction machines have taken over the majority of industrial applications in the modern world, has led to a rise in demand for efficient and reliable monitoring methods. This demand has been served over the years with different efficient monitoring techniques combined with diagnostic methods and Finite Element Analysis (FEA), using measurements of either stator currents or voltages, speed or torque ripples and magnetic field related quantities [1]-[4]. The latter case has been developed during the last years, making use of modern signal processing methods to assess fault conditions during both the start-up transient and the steady state [5], [6].

The Stray Flux Signal Analysis (SFSA) is in direct competition with the conventional Motor Current Signature Analysis (MCSA). SFSA has been applied with success on various types of faults [7]-[11]. For this type of analysis, magnetic flux that strays outside the motor is monitored by capturing the voltage induced on rigid search coils, sized inversely proportional to the machine's height [7], [10]. This allows inspection of signatures over the frequency spectra according to the origin of stray flux, thus being axial flux [7], axial & radial flux [8]-[10] or pure radial flux [11]. Rotor, stator and supply related fault signatures have previously been studied for space and time dependent harmonics. The detection of such signatures is based on early and more recent studies, in which the theoretical, experimental and quantitative modelling of the harmonic and spectral content is provided [4]-[6], [12]-[15].

Rotor cage defects have been examined in [12] with the use of a multi-equational numerical model which evaluates the $(1-2s)f_s$ component as inefficient for some locations of a random broken bar fault. In [13], the broken bars sideband modulus has been used as a relative indicator to account for the speed ripple effect. Further, [14] introduces an analytical categorization of harmonics for different case studies of healthy cages. An interesting comparison of signal spectral analysis methods is also given by [15] for broken bar faults using observers and providing a descriptive analysis of internal and external diagnostic methods. An analytical approach for the stator related frequencies under bar breakages is provided in [16] and is achieved through the experimental investigation of the sidebands of the 1st, 5th and 7th harmonic. Last, a comprehensive review of advanced diagnostics and methods for fault detection is given in [17].

Extensive research on the position and non-adjacency of the bar breakages has been undertaken in [18]-[25]. The reason for this interest lies in the fact that the physical mechanisms of these faults evolve undetected and they vary for real condition industrial case scenarios, as they can depend on the machine design and rotor construction [2], [4], [20]-[21]. As explained in [18], using a simplified model, non-adjacent broken bars can lead to misdiagnosis or masking of the fault, when two faulty bars are located within half pole pitch, leading to false negative diagnosis. The same work addresses that when multiple odd breakages are spotted within one complete pole's pitch, the fault can be partially masked and misinterpreted as a case with broken bars at adjacency. A similar analysis is provided in [19], examining the case where bars with breakage are in cross-diametrical positions for a four pole induction machine.

The influence of non-successive breakages on MCSA

Commented [NL1]: Einai logotexniko? 😉

P.A. Panagiotou, I. Arvanitakis, N. Lophitis & K.N Gyftakis are with the School of CEM and Research Institute for Future Transport & Cities, Coventry University, Coventry, UK (e-mail: k.n.gyftakis@ieee.org).

J. A. Antonino-Daviu is with the the Instituto Tecnológico de la Energía, Universitat Politècnica de València, Valencia, SPAIN (e-mail: joanda@die.upv.es).

implementation and reliability is examined in [20] by the application of the fault current approach and space-vector theory. Also, in [21] the authors reliably detect rotor asymmetries using signal decomposition during the transient regime for cases of industrial applications previously diagnosed as false-negative with MCSA. Further, in [22] and [23] the diagnostic potential of the zero sequence current (ZSC) is validated for cases of broken bars being adjacent and not respectively, while [24] introduces an indicator for detection of non-serial breakages using the Filtered Park's Vector Approach (FPVA). A compelling evaluation of high-order fault related harmonics is delivered by [25] for cases of double bar faults.

Regarding methods for signal analysis during machine operation, advanced signal processing techniques based on time-frequency distributions (TFD) have been proposed recently [26]-[33]. These techniques provide the representation of a signal on the joint time-frequency plane, allowing its decomposition, in order to study frequency transitions in time and observe oscillatory harmonic components and how they evolve. These include the Discrete Wavelet Transform (DWT) [21], [27] which can include the use of complex wavelets [28], while high-resolution spectral analysis techniques like the MUSIC algorithm have also been proposed [29].

To the same direction, a reconfigurable monitoring device is presented in [30], aiming for diagnosis of industrial equipment through application of DWT and Short-Time Fourier Transform (STFT). The latter is successfully used in [31], combined with notch filters, for detection of lubrication and bearing faults. The STFT is also utilized in [32] for speed estimation through current space vector amplitudes fluctuation, and in [33] for an approach on the same basis. Although there exists a trade-off between time and frequency resolution [29], STFT is frequently preferred due to its simplicity, low computational complexity and commercial availability in software packages.

In this work, the behavior of the stray flux spectral components of a 6-pole squirrel-cage induction motor with nominal characteristics $6.6\,kV$, $1.1\,MW$ at $50Hz$ are analyzed and studied using 2D FEM [49]. Healthy and faulty motors are assessed, including various faulty cases of adjacent and non-adjacent broken bars. With STFT the stray flux spectral content is represented on a Time-Frequency (T-F) spectrogram. Because the contours and their trajectories respond periodically as oscillations in time, their spectral densities calculated by the STFT is extracted and their own normalized FFT examined. The frequency content of the trajectories at steady state allowed to draw a cogent conclusion regarding their behavior in the time and frequency domain and how the fault frequencies carried in the signal of stray flux are modulated during the fault. This method improves the diagnostic ability of SFSA when the fault occurs in non-consecutive positions. The diagnostic validity of the proposed method is also demonstrated experimentally with laboratory tests on a 4-pole, $50\,Hz$ induction motor of $1.1\,kW$ output power.

II. Theoretical Background

A. Radial SFSA & Broken Bar Fault Signatures

There have been multiple examples where radial stray flux measurements have been used[8]-[11]. For a broken bar and one inter-turn short circuit, the medium frequency emission harmonic components, and the physical mechanisms causing them, are extensively described in [11]. A similar approach, focusing on the low frequency components, is introduced in [35] for the examination of eccentricity and broken bar faults. The same rotor faults are studied in [36]-[38] using internal Hall-effect flux sensors, providing an assiduous analytical description of the air-gap flux space harmonics. Also, stray flux signature analysis is applied for bar breakages in [39] & [40], and in [41]-[43] for bearing fault detection using also a statistical based approach. The diagnostic technique of stray flux analysis has been implemented successfully in [44] with application of the DWT and for separation of rotor faults from low frequency load oscillations in [45]. In the latest years, stray magnetic flux is being investigated under transient conditions as well [46]-[48]. Finally, comprehensive reviews on SFSA and state of the art diagnostics using these methods are provided in [49] and [50].

When a bar breakage occurs, a backward rotating magnetic field is generated due to the open-circuited bar and the lack of inter-bar and eddy currents in the point of breakage creating in the rotor cage an asymmetry that is clearly reflected in the motor's harmonic content [6], [11], [35]-[38]. This fault asymmetry is known to cause additional frequency sidebands, distanced by multiples of the motor's slip s from the fundamental frequency f_s and its multiples [21], [36]. These appear in the spectrum of stator-related quantities (stator current or stray flux), modulated by the component $(1-s)f_s$ because of the continuous induction from the rotor to the stator and vice-versa. The equation for these fault related sideband signatures is the following [36], [37]:

$$f_{bb} = [\tfrac{k}{p}(1-s) \pm s]f_s, \tag{1}$$

p being the number of pole pairs and $k \in \mathbb{Z}$ such that k/p is always an integer.

The problem is that in large induction motors, like the one under analysis with FEM in this paper, these fault signature sidebands lie very close to the fundamental frequency because of the rotor's speed being very close to the synchronous one, thus the low value of slip s at steady state [38]. This fact can complicate the diagnostic process and make it very difficult to detect the fault with accuracy, especially in the classical FFT where the spectral leakage of the windowing function is already an issue to encounter. Therefore, the sideband signatures of the 5th and 7th harmonic will be investigated in this work, since they are standing off at the distances $-4sf_s$ and $-6sf_s$ for the 5th and at $-6sf_s$ and $-8sf_s$ for the 7th harmonic. Those harmonics originate from the equation (1) above. This is because the sensor is placed on the stator and thus is considered static, resulting in sensing the same fault related harmonics around the stator space harmonics, similarly with the stator winding.

In the next Section (III-B), the STFT is applied on the radial stray flux signals of the motors presented from FEM in Section III-A. To aim for a more accurate diagnosis, the trajectories of the aforementioned sidebands regarding the 5th and 7th

harmonic are extracted and individualized on the time-frequency plane of the spectrogram. Then, using the transformation result at steady state, the FFT is applied on the extracted trajectory to evaluate its behavior as well as the oscillations related to the adjacency of the broken bar fault.

B. The Short-Time Fourier Transform

As introduced in the previous Section, the STFT offers a time-frequency representation of a signal by picturing the signals' spectral characteristics over time. The frequencies' spectral energy density is visualized by the spectrogram, which yields a contour plot of the magnitude. The contour plot is color-coded in a scale that expresses the intensity of the signal's spectral energy magnitude [31]-[33].

The continuous time STFT $X(t, f)$ of a signal is a function of both time t and frequency f –as opposed to the classical FFT that represents the signals' harmonic content as a function of frequency only– that can be computed from the FFT over a sliding window by the following equation [34]:

$$X(t,f) = \int_{-\infty}^{+\infty} x(t)w(t-\tau)e^{-j2\pi ft}dt \qquad (2)$$

where $x(t)$ is the signal of our interest, $w(t)$ is the sliding window, τ is the window shifting factor and $f = 2\pi/\omega$ the frequency. Equation (2) provides the joint time-frequency representation, as previously discussed, by means of the spectrogram:

$$S(t,f) = |X(t,f)|^2 \qquad (3)$$

C. Spectral Components Extraction

For the analysis of the studied signals, the discrete time STFT is implemented [34]. A Kaiser-Bessel window of length $L = 3972$ is selected as the sliding window function, with parameter $\beta = 40$ and 80% overlap between the time-frames. This ad-hoc selection accrued from fine tuning of the parameters accounting for two factors: to achieve a windowing with a response as close as possible to rectangular, and secondly to yield a good trade-off between time and frequency resolution to observe the harmonic trajectories in the spectrogram [15], [31].

Because of the low slip value and the problem of spectral leakage described previously, focus will be given to the sidebands of the higher harmonics at $250\ Hz$ (5th harmonic) and $350\ Hz$ (7th harmonic). In order to individualize the $(5-4s)f_s$ and $(5-6s)f_s$ components and the $(7-6s)f_s$ and $(7-8s)f_s$ components, the average value of slip at steady state is used, as well as the spectrograms shown in Fig. 1.

In the spectrograms of Fig. 1, the frequency components are pointed with dashed lines for two of the cases examined with the proposed analysis under FEM. The broken bar fault related components are used to derive from Eq. 3 their spectral content of fixed constant frequency over time as follows:

$$S\,(t, f_{a,i}) = |X(t, f_{a,i})|^2, \qquad (4)$$

where each component $f_{a,i}$ regards the *a-th* harmonic of interest and $i = 1, 2$.

For a clearer picture and better visualization of the trajectories' ripples, Fig. 2 depicts the spectrogram of the stray flux for Case #2 of Fig. 1a in the frequency area of the 5th harmonic before dimension reduction.

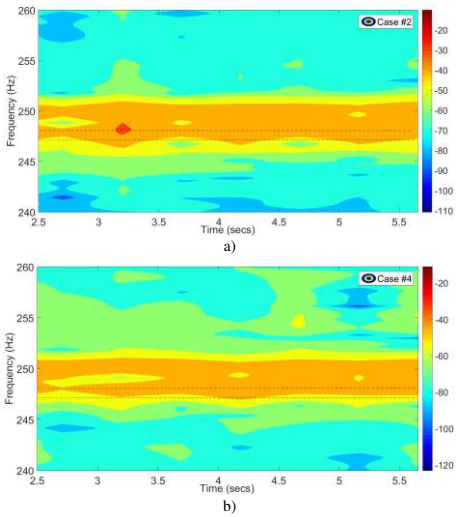

Fig. 1. Spectrogram for the freq. area of the stray flux 5th harmonic for two of the broken bar motors examined with FEM: a) Case #2 and b) Case #4. Frequency resolution $\Delta f = 0.91\ Hz$.

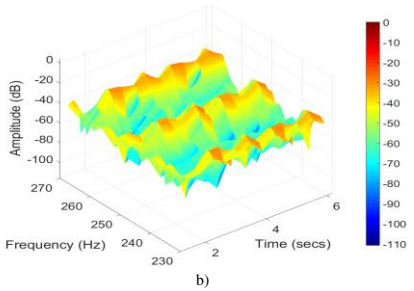

Fig. 2. STFT Spectrogram of Case #2 for the frequency area of the 5th harmonic. Frequency resolution $\Delta f = 1.41\ Hz$.

III. Finite Element Simulations

A. FEM Models

For the FEM validation, the electromagnetic analysis of an industrial Y-connected, 6-pole, $6.6\ kV$, $1.1\ MW$, $50\ Hz$ cage induction motor has been simulated with the software MagNet from Infologic/Mentor Graphics of Siemens Corporation. The rotor cage has been designed with 70 copper bars and the stator with 54 slots and a double layer 12-turn per slot 1-9 pitched winding. The healthy motor is depicted in Fig. 3a and the corresponding magnetic field in Fig. 3b. Details of the modelled motor is given in Table I. The flux sensor is a stranded 50-turn search coil, with the input and output wounded on a point of the machine's periphery close to the stator frame (Fig. 3a). A high resistance has been placed in series with the corresponding bars

to model the open circuit implied by the breakages and emulate the fault in 2D FEM.

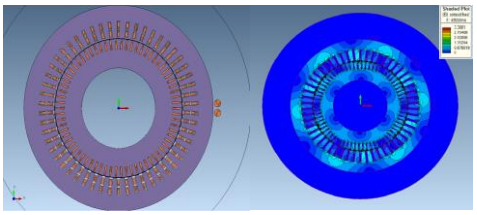

a) b)

Fig. 3. a) Healthy motor and b) magnetic field distribution of healthy motor.

TABLE I
SIMULATION CHARACTERISTICS OF THE MOTOR UNDER STUDY

Characteristics	Value
Supply frequency	50 Hz
Stator Connection	Y
Output power	1.1 MW
Rated Voltage	6.6 kV
Rated Current	170 A
Number of pole pairs	3
Rated speed	990 rpm
Number of stator slots	54
Number of rotor bars	70

Besides the healthy motor, three more cases have been simulated and studied. These account for cage breakages at different locations: one case of two adjacent broken bars and two cases of non-adjacent broken bars. All motors serve the same constant mechanical load of $11\,kN \cdot m$ at steady state (full load condition). To aid the reader, the four distinct FEM cases are labeled and referred to as $Case\ \#1$ to $Case\ \#4$. The cases are summarized in Table II along with the value of slip for each one of them, and the motors under the broken bar fault with the asymmetry in the corresponding magnetic flux density distribution are shown in Fig. 4. The time step of the transient FEA simulations has been 0.1 ms, which implies a sampling frequency of 10 kHz. As a result, this frequency is used for the signal acquisition of the extracted flux waveforms.

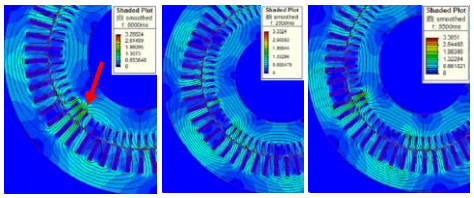

a) b) c)

Fig. 4. a) Motors under simulation & analysis: a) Case #2, b) Case #3 and c) Case #4.

TABLE II
CASE STUDIES

Case	Broken Bars	Location	Slip (%)
#1	healthy	–	0.91
#2	1&2	Adjacent	0.95
#3	1&6	Within half pole pitch	0.96
#4	1&11	Within one pole pitch	0.94

From Fig. 4, one can see that the broken bar fault asymmetry is not easily distinguished and observed in the magnetic field distribution for $Case\ \#3$ and $Case\ \#4$. The opposite is observed for $Case\ \#2$, which comes in agreement with the observations stated in [18] for the fault taking place at such positions. In addition, the FFT on the radial stray flux signal of $Case\ \#1$ (blue), $Case\ \#2$ (red) and $Case\ \#3$ (black) is shown in Fig. 5-a for the frequency area around the fundamental 50 Hz harmonic, where the closeness of the broken bar sidebands to f_s is noted. Fig. 5-b shows the STFT around the same frequency area, pointing the difficulty to observe the sidebands on the T-F plane because of their small distance from f_s and its spectral leakage overlap.

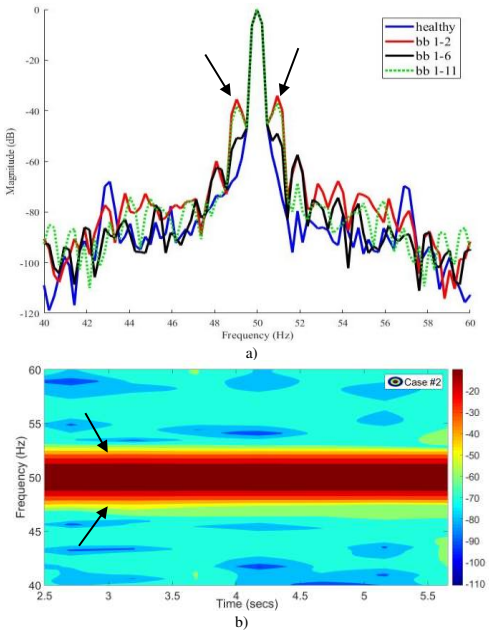

a)

b)

Fig. 5. a) FFT with freq. resolution $\Delta f = 0.91\ Hz$ of Case #1 (blue), Case #2 (red) and Case #3 (black) and b) STFT with freq. resolution $\Delta f = 1.11\ Hz$ of Case #2 in the frequency area of the fundamental f_s.

B. FEM Results

Considering $S(t, f_{5,i})$ the set of trajectories regarding the 5th harmonic and $S(t, f_{7,i})$ the set of trajectories regarding the 7th, let $S(t, f_{5,1})$ be the color-coded varying magnitude of the ripple expressed by the $(5-4s)f_s$ trajectory and $S(t, f_{5,2})$ be the one expressed by the $(5-6s)f_s$. Respectively, $S(t, f_{7,1})$ corresponds to the $(7-6s)f_s$ component, while $S(t, f_{7,2})$

corresponds to the $(7-8s)f_s$ component. These localized frequencies are extracted and evaluated in the time and then the frequency domain to observe how they are modulated. To characterize their modulations, the FFT is applied to each extracted time-signal $S(t, f_{a,i})$ of each case, considering the part of the signal that belongs to the steady state $(t \geq 1.5\ sec)$. The signals $S(t, f_{5,2})$ and $S(t, f_{7,2})$ are shown in Fig. 6 for the 5th (Fig. 6-a) and 7th (Fig. 6-c) harmonics' lower sidebands respectively for all cases.

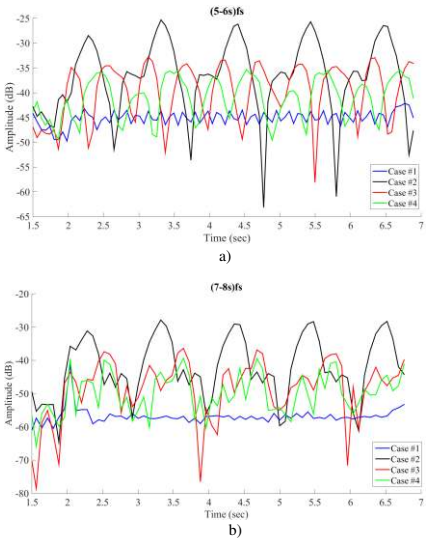

Fig. 6. The time-signals of $S(t, f_{a,2})$ for the lower sidebands of all cases at the frequencies: a) *(5-6s)fs* and b) *(7-8s)fs*.

A first observation noted from Fig. 6 for all cases, is that the frequency components of the healthy motor are characterized by much smaller amplitudes, compared to the faulty cases. Also, these frequencies behave as mono-component signals, with no significant oscillations -except for a very smooth ripple- and without carrying any slow evolving frequency components. This is not the case for the motors with broken bars though, where it is clearly observed that a dilatory frequency is included in the main signal. The latter indicates the presence of a rotor related fault - these signals appear as multi-component carrier-plus-sideband signals which in turn implies strong modulations due to the fault existence. Fig. 7 and Fig. 8 depict the corresponding FFT spectra of each signal of the $S(t, f_{5,i})$ and $S(t, f_{7,i})$ for all cases at the 5th and 7th harmonic. The amplitudes of all observed components presented in Fig. 7 and Fig. 8 are summarized in Tables III and IV.

TABLE III
FFT AMPLITUDES OF THE 5TH HARMONIC'S EXTRACTED COMPONENTS

Case	$5fs - 4sf_s$		$5fs - 6sf_s$	
	$4sf_s$	$6sf_s$	$4sf_s$	$6sf_s$
#1	-50 dB	-51.89 dB	-49.6 dB	-52.38 dB
#2	-22.49 dB	-26.88 dB	-22.93 dB	-27.21 dB
#3	-22.79 dB	-33.92 dB	-23.00 dB	-34.62 dB
#4	-25.35 dB	-35.27 dB	-25.44 dB	-35.26 dB

TABLE IV
FFT AMPLITUDES OF THE 7TH HARMONIC'S EXTRACTED COMPONENTS

Case	$7fs - 6sf_s$		$7fs - 8sf_s$	
	$6sf_s$	$8sf_s$	$6sf_s$	$8sf_s$
#1	-50 dB	-54.07 dB	-50.94 dB	-53.89 dB
#2	-28.11 dB	-31.21 dB	-28.32 dB	-31.85 dB
#3	-38.34 dB	-30.96 dB	-34.51 dB	-28.70 dB
#4	-36.45 dB	-34.82 dB	-36.09 dB	-35.82 dB

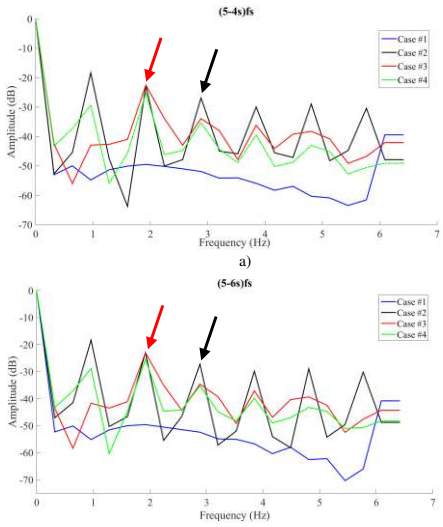

Fig. 7. FFT spectra of each $S(t, f_{5,i})$ for all cases for the spectral components: a) *(5-4s)fs* and b) *(5-6s)fs*. $\Delta f = 0.4\ Hz$.

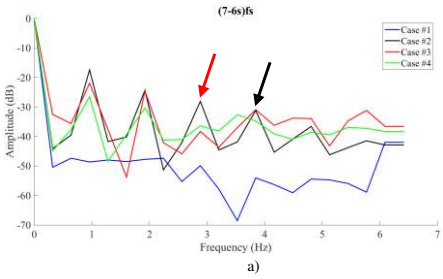

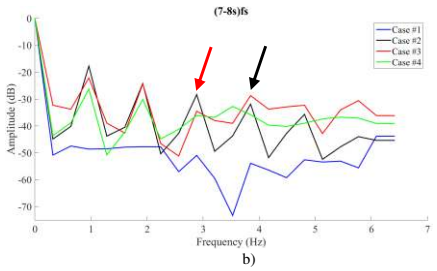

b)

Fig. 8. FFT spectra of each $S(t, f_{7,1})$ for all cases for the spectral components: a) *(7-6s)fs* and b) *(7-8s)fs*. $\Delta f = 0.4\ Hz$.

An inspection of the spectra in Fig. 7 provides a straight forward indication that a rotor fault has occurred, since the amplitudes of the faulty motors range for the first set from $-25.35\ dB$ to $-22.49\ dB$ (2nd column of Table III) and having increased with respect to the healthy motor, which is stabilized at approximately $-50\ dB$. Also, the FFT spectra of Fig. 7 reveal a spectral signature at $2\ Hz$ (red arrows). This signature practically corresponds to the $4sf_s$ sideband, where all the faulty cases have very similar amplitudes. This is a significant observation to report, since the fault signature at this frequency is showing the same result about the fault, regardless the position of the broken bars. The amplitude of this component regarding the $(5-6s)f_s$ ranges from $-25.44\ dB$ to $-22.93\ dB$ (4th column of Table III). Similar is the behavior of the component at $6sf_s$ illustrated at $3\ Hz$ (black arrows), where the faulty models approach an amplitude ranging from $-35.27\ dB$ to $-26.88\ dB$ for the second set (3rd column of Table III) and from $-35.27\ dB$ to $-27.21\ dB$ for the fourth set (5th column of Table III). At this frequency $Case\ \#2$ makes the only exception, where the signature's amplitude is elevated at a maximum level, because of the greater fault severity caused by the breakage adjacency that creates a greater local magnetic field asymetry.

An examination of Fig. 8 aims to harvest information about the fault through the $6sf_s$ component (red arrows) and the component at $8sf_s$ (black arrows). Both frequencies depicted in Fig. 8-a and Fig. 8-b are affected by the $6sf_s$ component, reaching amplitudes increase of $21.89\ dB$ ($Case\ \#2$), $11.66\ dB$ ($Case\ \#3$) and $13.55\ dB$ ($Case\ \#4$) with respect to the healthy motor for the first set (Table IV, 2nd column). Same levels of increase in the amplitudes are observed for the 3rd set affected by this subcomponent (Table IV, 4th column). Again, the case of adjacent broken bars exceeds all other amplitudes, having increased $6.19\ dB$ and $7.77\ dB$ more than $Case\ \#3$ and $Case\ \#4$ respectively.

Finally, it is compelling how the two frequencies shown in Fig. 8 respond to the $8sf_s$ commponent, which gives a satisfying alarm level for the fault occuring at the distance of half pole pitch ($Case\ \#3$) and one complete pole pitch ($Case\ \#4$). As it can be seen from the 3rd and 5th columns of Table IV, these subcomponent frequencies raise for all presented cases a noticeable alarm level –at least at full load condition– for the broken bar fault, both by their general morphology over the frequency spectra as well as by their amplitude levels compared to the healthy motor. This reliably confronts the problem of non-adjacent bar breakages and situates the fault able to be diagnosed as a rotor electrical fault, by taking advantage of the spectrogram's ripples and periodicities implied through the fault periodicity over the rotation of the rotor and the continuous stator to rotor induction.

IV. Experimental Setup & Validation

A. *Description of the experimental test-bed*

Fig. 9 depicts the laboratory test-bed used for experimental measurements of stray magnetic flux on a 4-pole, $50\ Hz$, $230\ V$, $1.1\ kW$ induction motor. As in the case of the FE simulations, the flux sensor is placed in a lateral position close to the stator frame accounting for portions of radial stray flux (Fig. 9-a). In Fig. 9-b the healthy rotor is depicted, along with the rotors used for emulating the broken bar fault by drilling holes in the positions of interest. The characteristics of the motor are presented in Table V, while all experimental cases are summarized in Table VI in accordance with the FEM cases presented in Table II.

TABLE V
Characteristics of The Experimental Motor

Characteristics	Value
Supply frequency	50 Hz
Stator Connection	Δ
Output power	1.1. kW
Rated Voltage	230 V
Rated Current	4.5 A
Number of pole pairs	2
Rated speed	1410 rpm
Number of stator slots	36
Number of rotor bars	28

a

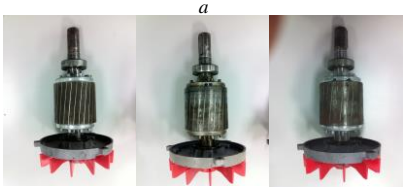

b

Fig. 9. Experimental set up of the 1.1 kW induction motor used for the experiments: a) Flux sensor in the position of interest, b) healthy rotor (left), rotor with 2 adjacent broken bars (middle) and one of the rotors with broken bars at non-adjacent positions (right) within half pole pitch.

The experimental cases are labeled and referred to as $Case\ \#1$ to $Case\ \#4$, respectively with the FEM cases. As described in Table V, the rotor cage of this motor consists of 28 rotor bars and the stator of 36 stator slots. It should be noted

that, since it is a 4-pole machine that is dealt with in the experimental approach, the position of the broken bars for $Case\ \#3$ & $Case\ \#4$ have been chosen to correspond as close as possible to the breakage scenario of distances within half pole pitch and one complete pole pitch.

TABLE VI
CASE STUDIES

Case	Broken Bars	Location	Slip (%)
#1	healthy	–	1.28
#2	1&2	Adjacent	1.21
#3	1&4	Within half pole pitch	0.92
#4	1&6	Within one pole pitch	0.84

B. Analysis of experimental results

The same trajectories as extracted and studied for the FEM models will be analyzed for the experimental measurements, which were taken on the test-bed described in Paragraph IV-A. Considering the $S(t, f_{5,i})$ and the $S(t, f_{7,i})$ family of trajectories, exactly as in Section III-B, the FFT spectra of the extracted components are shown in Fig. 10 & 11.

A first observation noted from Fig. 10 and Fig. 11, is that the healthy motor's spectra are characterized by existing fault related signatures but of lower amplitudes compared to the faulty motors. The main reason for their existence are the inherent manufacturing defects like the cage porosity or the laminations' magnetic anisotropy, which are always present in small laboratory motors of this capacity. This is reasonable and expected to come across with, since the FE simulations provide a theoretically ideal model where no inherent asymmetries or manufacturing defects are accounted for. However, neither the ideal FEM conditions nor the inherent asymmetries and manufacturing anomalies in the experimental motor disallow the application or effectiveness of the proposed method. The amplitudes of all observed components presented in Fig. 10 and Fig. 11 are summarized in Tables VII and VIII.

TABLE VII
FFT AMPLITUDES OF THE 5TH HARMONIC'S EXTRACTED COMPONENTS

Case	$5fs - 4sf_s$		$5fs - 6sf_s$	
	$4sf_s$	$6sf_s$	$4sf_s$	$6sf_s$
#1	-33.32 dB	-37.25 dB	-31.43 dB	-35.07 dB
#2	-21.32 dB	-33.40 dB	-21.29 dB	-33.54 dB
#3	-14.39 dB	–	-13.09 dB	–
#4	-14.43 dB	-26.04 dB	-24.54 dB	-27.26 dB

TABLE VIII
FFT AMPLITUDES OF THE 7TH HARMONIC'S EXTRACTED COMPONENTS

Case	$7fs - 6sf_s$		$7fs - 8sf_s$	
	$6sf_s$	$8sf_s$	$6sf_s$	$8sf_s$
#1	-46.85 dB	-56.29 dB	-44.85 dB	-56.29 dB
#2	-21.51 dB	-40.84 dB	-19.41 dB	-37.09 dB
#3	-17.13 dB	-24.93 dB	-15.18 dB	-22.72 dB
#4	-16.82 dB	-22.82 dB	-14.64 dB	-20.36 dB

In the spectra of Fig. 10, the expected $2ksf_s$ subcomponents are designated at the frequencies of $4sf_s$ and $6sf_s$ for the 5th harmonics components (black arrows), while from the second column of Table VII it is evident that the $S(t, f_{5,1})$ extracted trajectories have a difference of 12 dB ($Case\ \#2$), 18.93 dB ($Case\ \#3$) and 18.89 dB ($Case\ \#4$) with respect to the healthy case. The same amplitudes for the $4sf_s$ sub-component shown in the fourth column of Table VII, undergo an increase of

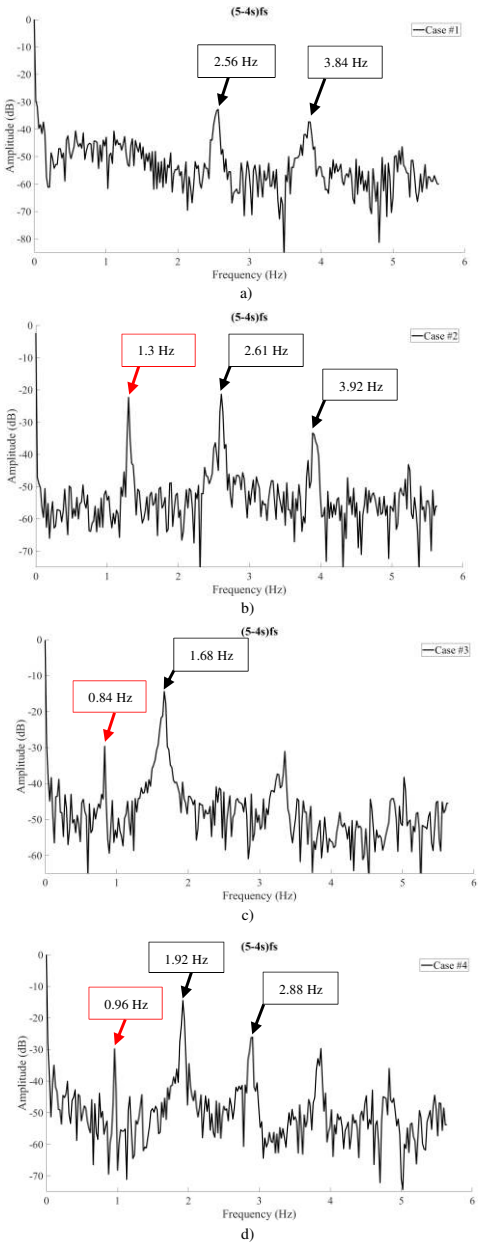

Fig. 10. FFT spectra of each $S(t, f_{5,1})$ for the spectral component $(5\text{-}4s)fs$ of: a) Case #1 b) Case #2 c) Case #3 d) Case #4. $\Delta f = 0.5\ Hz$.

$10.14\ dB$ ($Case$ #2), $18.34\ dB$ ($Case$ #3) and $6.89\ dB$ ($Case$ #4) with respect to the healthy case.

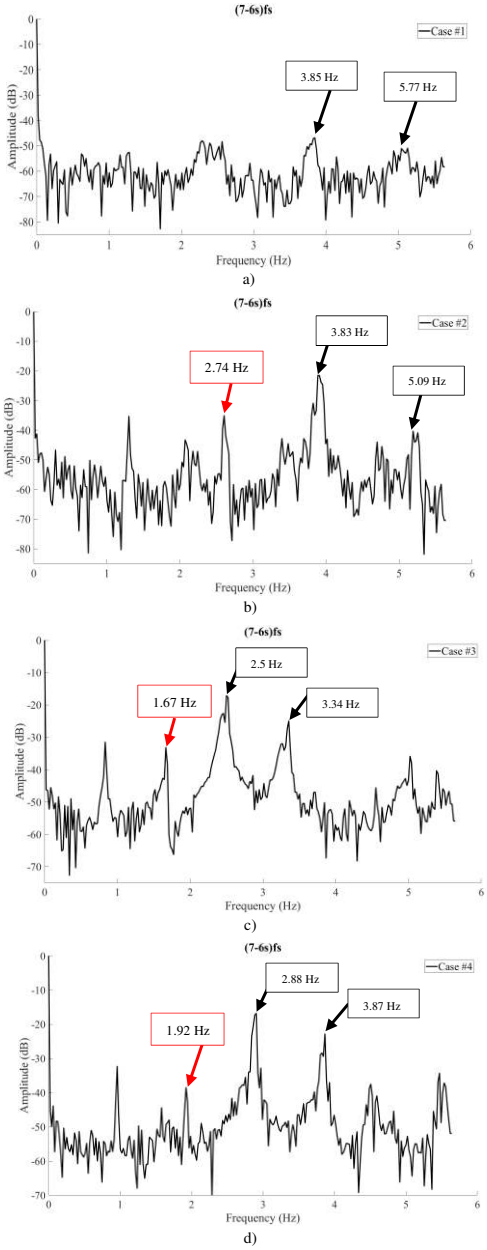

Fig. 11. FFT spectra of each $S(t, f_{s,2})$ for the spectral component *(5-6s)fs* of: a) Case #1 b) Case #2 c) Case #3 d) Case #4. $\Delta f = 0.5\ Hz$.

The most important fact to observe when comparing $Case$ #1 (healthy) with the rest of the cases, is that the spectral signature at $2sf_s$ (red arrows) is never present in the healthy motor's spectra around its fifth harmonic. The absence of this signature is also noticeable in the spectra of the extracted trajectories obtained from the FEM models (Fig 7). This offers the advantage to decipher the subcomponent arising at $2ksf_s$ $(k = 1)$ -existent only in faulty motors- and which is a reaction to the fault normally not existing in motors with healthy cages. This signature exists due the speed-ripple effect caused by the broken bar fault during the interaction of the counter-rotating magnetic fields at $\pm sf_s$ and the chain reaction of speed ripple harmonics propagated at $4sf_s$. The amplitude of this fault related speed-ripple signature at the 5th harmonic is summarized for all cases in the second column of Table IX.

Comparison of the spectra for the extracted $S(t, f_{7,1})$ component (Fig. 11) yields through the second column of Table VIII an increase of $25.34\ dB$ ($Case$ #2), $29.27\ dB$ ($Case$ #3) and $30.03\ dB$ ($Case$ #4) with respect to the healthy motor. Through the fourth column of Table VIII, these differences stand at $25.44\ dB$ ($Case$ #2), $29.67\ dB$ ($Case$ #3) and $30.21\ dB$ ($Case$ #4) respectively. The amplitudes of the $8sf_s$ subcomponent regarding the $S(t, f_{7,1})$ trajectory exceed with respect to $Case$ #1 an increase of $15.45\ dB$ ($Case$ #2), $29.27\ dB$ ($Case$ #3) and $30.03\ dB$ ($Case$ #4), as shown in the third column of Table VIII. Regarding the same signature for the $S(t, f_{7,2})$, its amplitudes increase $19.2\ dB$ for $Case$ #2, $33.57\ dB$ for $Case$ #3 and $35.93\ dB$ for $Case$ #4, compared to the healthy motor's amplitude.

Similarly to the 5th harmonic, the speed ripple effect manifest itself in the 7th harmonic frequency area. The component at $4sf_s$ in both *7fs –6sf*$_s$ and *7fs –8sf*$_s$ spectra does not exist in the healthy motor, while it presents an important amplitude in all faulty cases. This specific component is due to the speed ripple effect and thus unaffected by inherent rotor cage electromagnetic asymmetries. The amplitude of the fault related speed-ripple signature at the 7th harmonic is summarized for all cases in the second column of Table IX. Note that for the healthy $Case$ #1 the amplitude values are vacant in Table IX, since this signature does not exist for a healthy rotor.

TABLE IX
SPEED-RIPPLE SUBCOMPONENTS AMPLITUDES

Harmonic:	*5fs –4sf*$_s$	*7fs –6sf*$_s$
Component:	*2sf*$_s$	*4sf*$_s$
Case #1	–	–
Case #2	-22.29 dB	-35.31 dB
Case #3	-29.61 dB	-31.47 dB
Case #4	-29.77 dB	-32.28 dB

V. CONCLUSIONS

This work presented a novel approach for the detection of rotor bar faults at steady state, independently from the fault's spatial distribution. The proposed method analyzes components originating from frequency extraction of stray flux signals. The information of their spectral density $S(t, f_{a,i})$ is initially extracted with the use of the Short-Time Fourier Transform for

the *a-th* harmonic of interest. Afterwards, these time signals are evaluated at each chosen and localized frequency, to observe how their amplitudes respond in time and -by application of the classical FFT- examine how they are modulated. Focus was given on the 5th and 7th harmonics' sidebands, due to their relative further distance from the central harmonic.

The results indicate that the subcomponents of the selected fault related harmonics offer a great diagnostic potential, especially when analyzed with the perspective of the proposed approach. It was shown that several subcomponents are immune to inherent cage electromagnetic asymmetries, while dependent only on the speed ripple effect. Furthermore, such subcomponents modulate the fault frequencies' amplitudes in a unique way, thus being invaluable for reliable condition monitoring and health assessment of induction motors. Finally, the proposed technique detects the broken bar fault, even when non-adjacent breakages are located within half or one complete pole pitch. This reliably confronts the problem of false-negative misdiagnosis, which has so far been known to occur due to the fault's masking when broken bars are located at such distances.

REFERENCES

[1] M. S. Elricki, Y. Porat, A. Alexandrovitz, "Leakage Field Changes of an Induction Motor as Indication of Nonsymmetric Supply", *IEEE Trans. Ind. and Gen. Appl.*, Vol. IGA-7, No. 6, Nov/Dec 1971.

[2] N. M. Elkasabgy, A. R. Eastham, G.E. Dawson, "The Detection of Broken Bars In The Cage Rotor of an Induction Machine", *Conf. Rec. of the IEEE IAS Ann. Meeting,* pp. 181-187, Vol. 1, 1988.

[3] G. B. Kliman, R. A. Koegl, J. Stein, R. D. Endicott, M. W. Madden, "Noninvasive Detection of Broken Rotor Bars in Operating Induction Motors", *IEEE Trans. on Energy Conversion,* Vol. 3, No. 4, pp. 873-89, Dec 1988.

[4] A. Bellini, F. Flippetti, G. Franceschini, C. Tassoni, G. B. Kliman, "Quantitative Evaluation of Induction Motor Broken Bars By Means of Electrical Signature Analysis", *Conf. Rec. of the 31st Ann. Meeting & World Conf. on Ind. Appl. of Electrical Energy,* pp. 484-491, Vol. 1, 2000.

[5] H. Henao, T. Assaf, G. A. Capolino, "Detection of Voltage Source Dissymmetry in an Induction Motor Using the Measurement of Axial Leakage Flux", *IEEE ICEM,* 2000.

[6] M. El H. Benbouzid, G. B. Kliman, "What Stator Current Processing-Based Technique to Use for Induction Motor Rotor Faults Diagnosis?", *IEEE Trans. on Energy Conv.,* Vol. 18, No. 2, pp. 238-244, June 2003.

[7] T. Assaf, H. Henao, G. A. Capolino, "Simplified Axial Flux Spectrum Method to Detect Incipient Stator Inter-Turn Short-Circuits in Induction Machine", *IEEE Int. Symposium on Ind. Electronics,* pp. 815-819, 2004.

[8] A. Yazidi, H. Henao, G. A. Capolino, "Broken Rotor Bars Fault Detection in Squirrel Cage Induction Machines", *IEEE Int. Conf. on Electric Machines & Drives,* pp. 741-747, 2005.

[9] S. H. Kia, H. Henao, G. A. Capolino, C. Martis, "Induction Machine Broken Bars Fault Detection Using Stray Flux after Supply Disconnection", *IEEE IECON,* pp. 1498-1503, 2006.

[10] A. Yazidi, H. Henao, G. A. Capolino, M. Artioli, F. Filippetti, D. Casadei, "Flux Signature Analysis: an Alternative Method for the Fault Diagnosis of Induction Machines", *IEEE Russia Power Tech,* pp. 1-6, 2005.

[11] R. Romary, R. Corton, D. Thailly, J. F. Brudny, "Induction Machine Fault Diagnosis Using an External Radial Flux Sensor", *The European Physical Journal-Applied Physics, 32 (2),* pp. 125-132, 2005.

[12] Tadeusz J. Sobczyk, Waclaw Maciolek, "Is the $(1-2s)f_0$ in Sator Currents Sufficient for Detection of Rotor Cage Faults?", *IEEE SDEMPED,* Vienna, Austria, pp.1-5, Sep. 2005.

[13] A. Bellini, C, Concari, G. Franceschini, E. Lorenzani, C. Tassoni, A. Toscani, "Thorough Understanding and Experimental Validation of Current Sideband Components in Induction Machines Rotor Monitoring", *IEEE IECON,* pp. 4957-4962, 2006.

[14] G. M. Joksmovic, J. Riger, T. M. Wolbank, N. Peric, M. Vasak, "Stator-Current Spectrum Signature of Healthy Cage Rotor Induction Machines", *IEEE Trans. on Ind. Electronics,* Vol. 60, No. 9, pp. 4025-4033, 2013.

[15] M. Eltabach, A, Charara, I. Zein, "A Comparison of External and Internal Methods of Signal Spectral Analysis for Broken Rotor bars Detection in Induction Machines", *IEEE Trans. on Ind. Electronics,* Vol. 51, No. 1, pp. 107-121, 2004.

[16] H. Henao, H. Razik, G.A. Capolino, "Analytical Approach of the Stator Current Frequency Harmonics Computation for Detection of Induction Machine Rotor Faults", *IEEE Trans. on Ind. App.,* Vol. 41, No. 3, pp. 801-807, 2005.

[17] A. Bellini, F. Filippetti, C. Tassoni, G.A. Capolino, "Advances in Diagnostic Techniques for Induction Machines", *IEEE Trans. on Ind. Electronics",* Vol. 55, No. 12, pp. 4109-4126, 2008.

[18] G. Y. Sizov, A. Sayed-Ahmed, C.C. Yeh, N. A. O. Demerdash, "Analysis and Diagnostics of Adjacent and Nonadjacent Broken-Rotor-Bar Faults in Squirrel-Cage Induction Machines", *IEEE Trans. on Ind. Electronics,* Vol. 56, No. 11, pp. 4627-4641, 2009.

[19] A. Menacer, G. Champenois, M. S. Nait Said, A. Benakcha, S. Moreau, S. Hassaine, "Rotor Failures Diagnosis of Squirrel Cage Induction Motors with Different Supplying Sources", *Journal of Elec. Eng. & Tech.,* Vol. 4, No. 2, pp. 219-228, 2009.

[20] M. Riera-Guasp, M. Fernandez Cabanas, J. A. Antonino-Daviu, M. Pineda-Sanchez, C. H. Rojas Garcia, "Influence of Nonconsecutive Bar Breakages in Motor Current Signature Analysis for the Diagnosis of Rotor Faults In Induction Motors", *IEEE Trans. on Energy Conv.,* Vol. 25, No. 1, pp. 80-89, 2011.

[21] J. A. Antonino-Daviu, S.B. Lee, E. Wiedenbrug, "Reliable detection of rotor bar failures in induction motors operating in petrochemical plants", *IEEE Petroleum & Chemical Industry Conf. Europe,* pp. 1-9, 2014.

[22] K. N. Gyftakis, J. A. Antonino-Daviu, R. Garcia-Hernandez, M. McCulloh, D. A. Howey, A. J. Marques-Cardoso, "Comparative Experimental Investigation of Broken Bar Fault Detectability in Induction Motors", *IEEE Trans. on Ind. App.*, Vol. *52*, No. 2, pp. 1452-1459, 2016.

[23] J. A. Antonino-Daviu, K. N. Gyftakis, R. Garcia-Hernandez, H. Razik, A. J. Marques-Cardoso, "Comparative Influence of Adjacent and Non-adjacent Broken Rotor Bars on the Induction Motor Diagnosis trough MCSA and ZSC Methods", *IEEE IECON,* pp. 001680-001685, 2015.

[24] K. N. Gyftakis, J. A. Antonino-Daviu, A. J. Marques-Cardoso, "A Reliable Indicator to Detect Non-Adjacent Broken Rotor Bars Severity in Induction Motors", *IEEE ICEM*, pp. 2910-2916, 2016.

[25] M. Riera-Guasp, J. Pons-Linares, F. Vedreno-Santos, J. A. Antonino-Daviu, M. Fernandez Cabanas, "Evaluation of the Amplitudes of High-Order Fault Related Components in Double Bar Faults", *IEEE SDEMPED,* pp. 307-315, 2011.

[26] J. A. Antonino-Daviu, V. Climente-Alarcon, J. Pons-Linares, M. Pineda-Sanchez, P. Jover-Rodriguez, A. Arkkio, "Application of TFD tools for the tracing of eccentricity-related components in induction machines", *IEEE IECON'09,* pp. 1039-1044*,* 2009.

[27] S. H. Kia, H. Henao, G. A. Capolino, "Diagnosis of Broken-Bar Fault in Induction Machines Using Discrete Wavelet Transform Without Slip Estimation", *IEEE Trans. on Ind. App.,* Vol. 45, No. 4, pp. 1395-1404, 2009.

[28] I. P. Tsoumas, G. Georgoulas, E. D. Mitronikas, A. N. Safacas, "Asynchronous Machine Rotor Fault Diagnosis Technique Using Complex Wavelets", *IEEE Trans. on Energy Conv.,* Vol. 23, No. 2, pp. 444-459, 2008.

[29] A. Garcia-Perez, R. J. Romero-Troncoso, E. Cabal-Yepez, R. A. Osornio-Rios, Jose de Jesus Rangel-Magdaleno, H. Miranda, "Startup Current Analysis of Incipient Broken Rotor Bar in Induction Motors using High-Resolution Spectral Analysis", *IEEE SDEMPED,* pp. 657-663, 2011.

[30] E. Cabal-Yepez, A. G. Garcia-Ramirez, R. J. Romero-Troncoso, A. Garcia-Perez, R. A. Osornio-Rios, "Reconfigurable Monitoring System for Time-Ferquency Analysis on Industrial Equipment Through STFT and DWT", *IEEE Trans. on Ind. Informatics,* Vol. 9, No. 2, pp. 760-71, 2013.

[31] M. Lopez-Ramirez, R. J. Romero-Troncoso, D. Morinigo-Sotelo, O. Duque-Perez, L. M. Ledesma-Carrillo, D. Camarena-Martinez, A. Garcia-Perez, " Detection and Diagnosis of Lubrication and Faults in Bearing on Induction Motors through STFT", *IEEE CONIELECOMP,* pp. 13-18, 2016.

[32] C. Wang, Z. Zhou, P. J. Unsworth, P. Igic, "Current Space Vector Amplitude Fluctuation based Sensorless Speed Measurement of Induction Machines Using Short Time Fourier Transformation", *IEEE IECON,* pp. 1869-1874, 2008.

[33] C. Wang, Z. Zhou, P.J. Unsworth, T. O'. Farrell, "Sensorless Speed Measurement of Induction Machines Using Short Time Fourier Transformation", *IEEE SPEEDAM*, pp. 1114-1119, 2008.
[34] K. Gröchenig. "Foundations of time-frequency analysis", Springer Science & Business Media, *2013*.
[35] A. Ceban, R. Pusca, R. Romary, "Eccentricity and Broken Rotor Bars Faults – Effects on the External Axial Field", *IEEE ICEM,* pp. 1-6, 2010.
[36] K. Saad, G. Mirzaeva, "Fault Diagnosis of Induction Motors by Space Harmonics Analysis of the Main Air Gap Flux", *IEEE ICEM*, pp. 1608-1613, 2014.
[37] K. Saad, G. Mirzaeva, "Advanced Diagnosis of Rotor Faults in Large Induction Motors Based on Internal Flux Measurement", *IEEE IAS Ann. Meeting,* pp. 1-8, 2016.
[38] K. Saad, G. Mirzaeva, "Space-Time Representation of the Main Air Gap Flux of a Three Phase Squirrel Cage Induction Motor and its Application to Detect Eccentricity", *IEEE IEMDC,* 2015.
[39] I. Chernyavska, O. Vitek, "Analysis of Broken Rotor Bar Fault in a Squirrel-Cage Induction Motor by Means of Stator Current and Stray Flu Measurement", *IEEE IPEMC,* pp. 532-537, 2016.
[40] P. Bernat, Z. Hytka, P. Kacor, "Indication of failures of rotor bar on induction machine with squirrel cage rotor in its external electromagnetic field", *IEEE 16th Int. Sci. Conf. on Electric Power Engineering (EPE)*, pp. 691-696, 2015.
[41] C. Harlisca, L. Szabo, L. Frosini, A. Albini, "Bearing Faults Detection in Induction Machines Based on Statistical Processing of the Stray Flux Measurements", *IEEE SDEMPED,* pp. 371-376, 2013.
[42] L. Frosini, M. Magnaghi, A. Albini, G. Magrotti, "A new diagnostic instrument to detect generalized roughness in rolling bearings for induction motors", *IEEE SDEMPED,* September 2015.
[43] L. Frosini, C. Harlişca, L. Szabó, "Induction machine bearing fault detection by means of statistical processing of the stray flux measurement", *IEEE Transactions on Industrial Electronics*, Vol. *62, No.* 3, pp.1846-1854, March 2015.
[44] L. Frosini, S. Zanazzo, A. Albini, "A wavelet-based technique to detect stator faults in inverter-fed induction motors", *IEEE ICEM 2016*, pp. 2917-2923, September 2016.
[45] T. Goktas, M. Arkan, M. S. Mamis, B. Akin, "Separation of Induction Motor Rotor Faults and Low Frequency Load Oscillations Through the Radial Leakage Flux", IEEE ECCE, pp. 3165-3170, Oct. 2017.
[46] J. A. Ramirez-Nunez, J. A. Antonino-Daviu, V. Climente-Alarcón, A. Quijano-López, H. Razik, R. A Osornio-Rios, R. J. Romero-Troncoso, "Evaluation of the detectability of electromechanical faults in induction motors via transient analysis of the stray flux", *IEEE Transactions on Industry Applications*, Vol 54, No. 5, pp. 4324-4332, Sep. 2018.
[47] Antonino-Daviu, J., Quijano-López, A., Climente-Alarcon, V. and Razik, H., 2017, October. Evaluation of the detectability of rotor faults and eccentricities in induction motors via transient analysis of the stray flux. In *Energy Conversion Congress and Exposition (ECCE), 2017 IEEE* (pp. 3559-3564). IEEE.
[48] Antonino-Daviu, J., Razik, H., Quijano-Lopez, A. and Climente-Alarcon, V., 2017, October. Detection of rotor faults via transient analysis of the external magnetic field. In *Industrial Electronics Society, IECON 2017-43rd Annual Conference of the IEEE* (pp. 3815-3821). IEEE.
[49] C. Jiang, S. Li, T.G. Habetler, "A review of condition monitoring of induction motors based on stray flux", *IEEE Energy Conversion Congress and Exposition (ECCE),* pp. 5424-5430, Oct. 2017.
[50] M. Riera-Guasp, J.A. Antonino-Daviu, G.A. Capolino, "Advances in Electrical Machine, Power Electronic, and Drive Condition Monitoring and Fault Detection: State of the Art", *IEEE Trans. Industrial Electronics*, Vol. 62, No. 3, pp.1746-1759, March 2015.
[51] P. A. Panagiotou, I. Arvanitakis, N. Lophitis , J. A. Antonino-Daviu, K. N. Gyftakis, "Analysis of Stray Flux Spectral Components in Induction Machines under Rotor Bar Breakages at Various Locations", *IEEE ICEM 2018*, pp. 2345-2351, Sep. 2018.